NASA/TM–20260000246

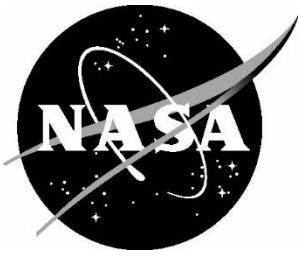

Experimental Characterization of the Material Properties of T700GC/LMPAEK Thermoplastic Composites for LS-DYNA MAT 213 Modeling

Jackob W. Black, Ryan G. Premo, and Han-Gyu Kim
Mississippi State University, Mississippi State, Mississippi

J. Michael Pereira, Trenton M. Ricks, and Robert K. Goldberg
Glenn Research Center, Cleveland, Ohio

Justin D. Littell
Langley Research Center, Hampton, Virginia

January 2026

NASA STI Program Report Series

Since its founding, NASA has been dedicated to the advancement of aeronautics and space science. The NASA scientific and technical information (STI) program plays a key part in helping NASA maintain this important role.

The NASA STI program operates under the auspices of the Agency Chief Information Officer. It collects, organizes, provides for archiving, and disseminates NASA's STI. The NASA STI program provides access to the NTRS Registered and its public interface, the NASA Technical Reports Server, thus providing one of the largest collections of aeronautical and space science STI in the world. Results are published in both non-NASA channels and by NASA in the NASA STI Report Series, which includes the following report types:

- TECHNICAL PUBLICATION. Reports of completed research or a major significant phase of research that present the results of NASA Programs and include extensive data or theoretical analysis. Includes compilations of significant scientific and technical data and information deemed to be of continuing reference value. NASA counterpart of peer-reviewed formal professional papers but has less stringent limitations on manuscript length and extent of graphic presentations.

- TECHNICAL MEMORANDUM. Scientific and technical findings that are preliminary or of specialized interest, e.g., quick release reports, working papers, and bibliographies that contain minimal annotation. Does not contain extensive analysis.

- CONTRACTOR REPORT. Scientific and technical findings by NASA-sponsored contractors and grantees.

- CONFERENCE PUBLICATION. Collected papers from scientific and technical conferences, symposia, seminars, or other meetings sponsored or co-sponsored by NASA.

- SPECIAL PUBLICATION. Scientific, technical, or historical information from NASA programs, projects, and missions, often concerned with subjects having substantial public interest.

- TECHNICAL TRANSLATION. English-language translations of foreign scientific and technical material pertinent to NASA's mission.

Specialized services also include organizing and publishing research results, distributing specialized research announcements and feeds, providing information desk and personal search support, and enabling data exchange services.

For more information about the NASA STI program, see the following:

- Access the NASA STI program home page at http://www.sti.nasa.gov

.

NASA/TM-20260000246

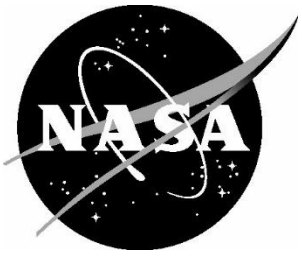

Experimental Characterization of the Material Properties of T700GC/LMPAEK Thermoplastic Composites for LS-DYNA MAT 213 Modeling

Jackob W. Black, Ryan G. Premo, and Han-Gyu Kim
Mississippi State University, Mississippi State, Mississippi

J. Michael Pereira, Trenton M. Ricks, and Robert K. Goldberg
Glenn Research Center, Cleveland, Ohio

Justin D. Littell
Langley Research Center, Hampton, Virginia

National Aeronautics and
Space Administration

Glenn Research Center
Cleveland, Ohio 44135

January 2026

Available from:

NASA STI Program / Mail Stop 050
NASA Langley Research Center
Hampton, VA 23681-2199

Acknowledgments

The material in this report is based upon work supported by NASA under Award number MS-80NSSC22M0206. The authors gratefully acknowledge the technical contributions of Sandi Miller at the NASA Glenn Research Center and Joe Capriotti at the Advanced Composites Institute, Mississippi State University.

Experimental Characterization of the Material Properties of T700GC/LMPAEK Thermoplastic Composites for LS-DYNA MAT 213 Modeling

Jackob Black, Ryan G. Premo, and Han-Gyu Kim
Mississippi State University
Mississippi State, Mississippi 39762

J. Michael Pereira, Trenton M. Ricks, and Robert K. Goldberg
National Aeronautics and Space Administration
Glenn Research Center
Cleveland, Ohio 44135

Justin D. Littell
National Aeronautics and Space Administration
Langley Research Center
Hampton, Virginia 23666

Abstract

The work in this report is focused on the development and execution of experimental frameworks to characterize the T700G/LM-PAEK thermoplastic composite material as required for progressive damage and failure analysis simulation and modeling in the MAT 213 material model. MAT 213 is a composite material model incorporated within the commercial transient dynamic finite element code LS-DYNA. MAT 213 requires scalar material properties such as moduli and Poisson's ratios, complete sets of stress-strain curves in a tabulated format, and plasticity flow rule coefficients to properly conduct the simulations. The experimental data obtained from in-plane mechanical testing presented in this report were obtained using multiple experimental techniques at a variety of length scales (i.e., macroscopic, microscopic, and hybrid) and extensively utilized digital image correlation. The data obtained from this experimental program was successfully utilized to calibrate the deformation sub-model of MAT 213. The complete work described in this report will contribute to the development of a MAT 213 input deck that will facilitate high-fidelity simulations of high-velocity ballistic impacts in composite materials.

1.0 Introduction

Space vehicles and aircraft structures can experience unexpected high-energy impact damage, as shown in the wing damage of space shuttle Columbia on the STS-107 mission (Ref. 1) and the fan blade-out impact damage to Southwest Airlines Boeing 737 aircraft (Ref. 2) in 2003 and 2018, respectively. While neither of these incidents occurred in structures that were made of polymer composites, there is a need to accurately simulate the impact damage that can occur in composite structures which are widely used in aerospace components. An advanced material model utilizing plasticity and damage parameters was developed by a consortium led by the Federal Aviation Administration (FAA) and the National Aeronautics and Space Administration (NASA) to be implemented into the commercial transient dynamic finite element software LS-DYNA (Ref. 3). This material model, commonly known as MAT 213, consists of deformation, damage and failure sub-models and possesses the capability of simulating high-speed impact, crash and

crush damage events in composite components and vehicles (Refs. 4-6). MAT 213 has been utilized to analyze a variety of composites subjected to dynamic loading conditions. For example, previous researchers conducted coupon-level characterization testing of an IM7/8552 carbon-fiber-reinforced polymer composite material (Refs. 7,8). This data was used to model the dynamic crush behavior of the material using MAT 213 (Ref. 9). In a similar fashion, the work described in this report is focused on characterizing Toray Cetex® TC1225 (Ref. 10) Low-Melt PolyArylEtherKetone (LMPAEK) reinforced by T700GC-12K unidirectional carbon-fiber (named T700GC/LMPAEK in this report) to obtain the data required to generate the input for MAT 213. As a specific form of PolyEtherEtherKetone (PEEK) and PolyEtherDiphenylEtherKetone (PEDEK) copolymer, LMPAEK thermoplastic materials were recently developed for increased production speed, wider processing tolerance, and enhanced interlayer adhesion compared to PEEK (Refs. 11-12). Extensive coupon testing of T700GC/LMPAEK was conducted by the National Center for Advanced Materials Performance (NCAMP), and the pointwise, scalar material properties of T700GC/LMPAEK were reported in an NCAMP test report (Ref. 13). The material input card of MAT 213, however, requires tabulated, complete stress-strain curves as input data. As the initial step towards simulating the dynamic crush behaviors of T700GC/LMPAEK using MAT 213, the work herein is focused on obtaining the experimental data required to build a material input card for MAT 213 with a specific focus on obtaining the data required for analyzing a structure using two-dimensional shell elements. Having the NCAMP data as the baseline for validation, the material properties and stress-strain data were obtained from in-plane tension, compression, and shear tests of T700GC/LMPAEK coupons. For the acquisition of the required experimental data, a 2D Digital Image Correlation (DIC) technique was employed in different scales. Most of the data was obtained from macroscale (or coupon-scale) DIC tests, while a microscopic DIC system was adopted for cases where the failure strains of the material were quite low (such as 90° tensile coupons). The microscopic data were particularly effective in characterizing the elastic and plastic Poisson's ratios of the material.

2.0 Test Matrix

Based on procedures outlined in the MAT 213 User Guide (Ref. 14), a test matrix was designed to obtain the experimental data required for shell element analyses using MAT 213. Using the test matrix, both the required tabulated data and scalar material properties could be obtained. Note that for two-dimensional shell element analyses, through-thickness (i.e., along the 3-direction principal axis) tensile and compressive data and transverse (i.e., in the 1-3 and 2-3 planes) shear data is not required. The coupons were designed following appropriate ASTM standards (Refs. 15-18). The test matrix, including the ASTM standards used to perform the tests, is presented in *Table 1*. In the table, the fiber direction of the specimens is indicated with the 1-direction principal axes, while the $x$geometric axes represent the loading (or longitudinal) directions for the tests. It needs to be noted that the 45° off-axis tension test (O12) is specified as optional for shell element analyses in the user guide. Additionally, the off-axis data required for input into MAT 213 is specified as needing to be obtained from tests of 45° laminates. However, in this work $\pm 45°$ laminates were tested following the ASTM D3518/D3518M-18 standard (Ref. 18). Thus, the off-axis data set was merely used as a reference. For shear data, MAT 213 requires only 2-1 in-plane data as input. However, the V-notch shear tests of this work included both 1-2 and 2-1 test sets as the ASTM manual specifies both directions, and NCAMP also performed 1-2 in-plane shear tests instead of 2-1 using an alternative test method. The additional 1-2 shear data set from this work was compared with the NCAMP data for validation and was also compared with the 2-1 strength data from this work.

Table 1. Test matrix required for the MAT 213 shell element

Test type	Loading & fiber directions	Layup	ASTM standards
Tension 1-direction (**T1**)	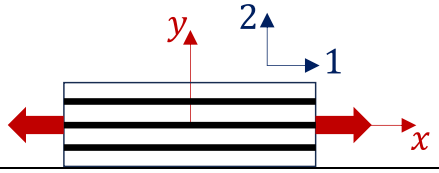	$[0]_8$	D3039/D3039M-17 (Ref. 15)
Tension 2-direction (**T2**)	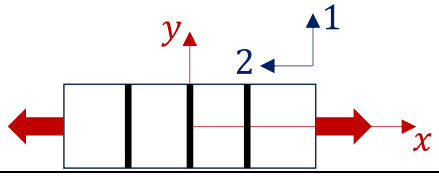	$[90]_{16}$	D3039/D3039M-17 (Ref. 15)
Compression 1-direction (**C1**)	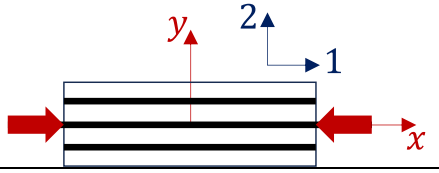	$[0]_{32}$	D6641/D6641M-23 (Ref. 16)
Compression 2-direction (**C2**)	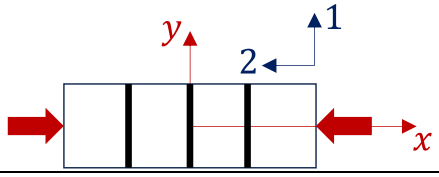	$[90]_{32}$	D6641/D6641M-23 (Ref. 16)
Shear 1-2 plane (**S12**)	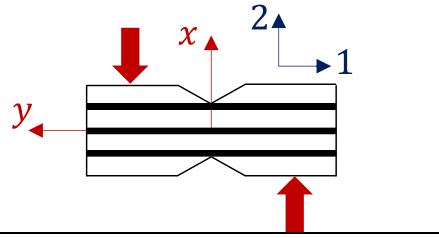	$[0]_{16}$	D5379/D5379M-19e1 (Ref. 17)
Shear 2-1 plane (**S21**)	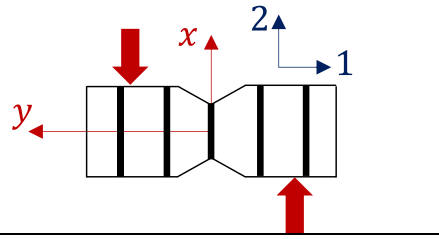	$[90]_{16}$	D5379/D5379M-19e1 (Ref. 17)
Off-axis tension (**O12**)	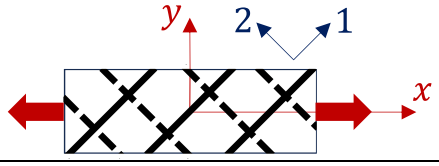	$[\pm 45]_{2s}$	D3518/D3518M-18 (Ref. 18)

3.0 Experimental Setup

3.1 Testing setup

The test sets listed in *Table 1* were conducted using two testing systems, as shown in Figure 1. The system that was used depended on the loading levels that were required for a particular test. A Shimadzu AGX V2 testing system (see *Figure 1a*) with a 300 kN frame capacity was employed for most of the tests, other than the V-notched shear tests S12 and S21. For the Shimadzu system, a Basler Ace 12-megapixel machine vision camera was used to capture digital images, which were analyzed for strain analysis using a Correlated Solutions VIC-2D DIC software package. A Psylotech uTS system (see *Figure 1b*), which can support up to 2 kN loading, was utilized with an Olympus BXFM microscope, a Basler Ace machine vision camera, and a VIC-2D DIC software package. The microscope and Psylotech system were used for the 90-degree tension tests. The macroscopic camera and Psylotech were used for the S12 and S21 shear tests. For all the other tests, the Shimadzu with the macroscopic camera was used.

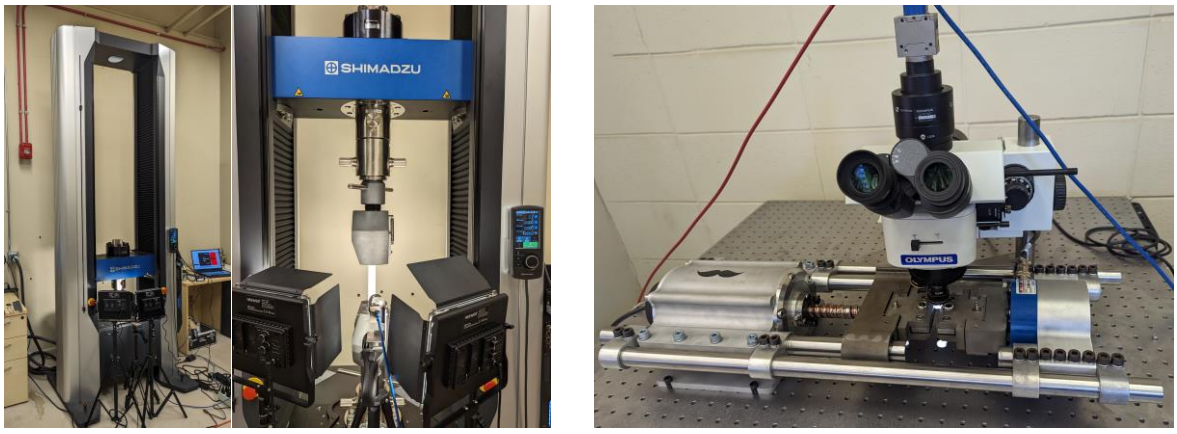

(a) (b)

Figure 1. Employed testing systems. (a) Shimadzu AGX V2 testing system. (b) Psylotech μTS testing system.

3.2 Specimen preparation

Following the layup designs specified in the text matrix shown in Table 1, 12-inch x 12-inch T700GC/LMPAEK panels were manufactured at the NASA Glenn Research Center. The details of the manufacturing process of the panels can be found in the report from Miller et al. (Ref. 19). Color images along with C-scans were taken immediately after the manufacturing process for quality control. Some images of a $[0]_8$ panel for the T1 tests (see Table 1) are shown in *Figure 2*. In the C-scan image (see *Figure 2b*), the solid red region indicates strong interlaminar bonding, while the blue and white areas represent weak bonding and debonding, respectively. Based on the C-scan images, potential defects were demarcated on the panels, as shown in *Figure 2a*. The test specimens were cut from the panels, avoiding the defective areas. The C-scan images of the other panels are presented in the Appendix.

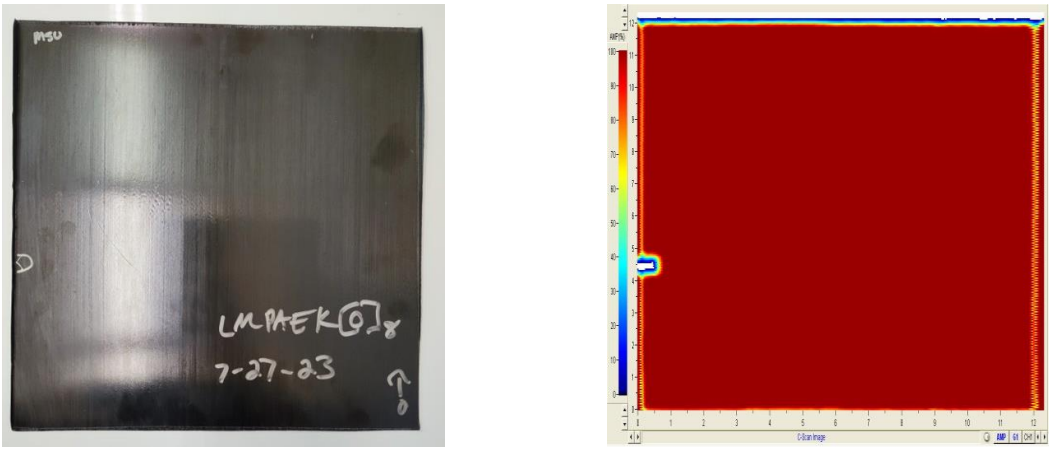

(a) (b)

Figure 2. Images of a $[0]_8$ panel for the T1 tests. (a) A panel image. (b) A C-scan image of the panel.

For the portion of the tensile tests conducted using the microscopic method, small rectangular specimens were cut from the panels and machined into dog-bone shapes (see *Figure 3a*). The dog-bone shapes were intended to have more friction between the specimens and the clamping fixtures (see *Figure 3b*) and to induce failure near the middle of the specimens. The macroscopic tension specimens (utilized for T1 and T2) had tabs following the ASTM specification in 3039/D3039M-17 (Ref. 15). For DIC data acquisition, the macroscopic and microscopic specimens had different scales of speckles on them, as shown in *Figure 4*. Random speckle patterns on the macroscopic specimens were generated using spray paints. Microscopic specimens (Utilized for T2), however, required significantly smaller speckles than the macroscopic ones, and thus, an airbrush was used to apply the speckles for microscopic DIC.

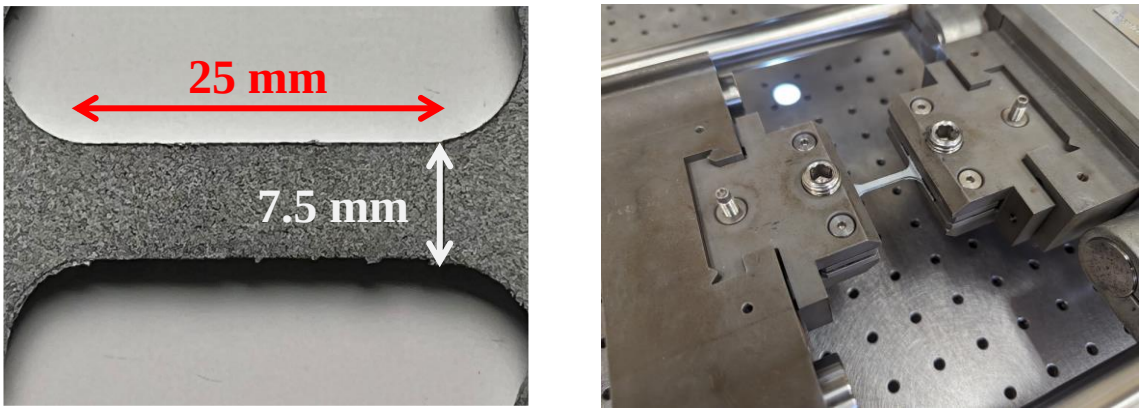

(a) (b)

Figure 3. Dog-bone specimens for the microscopic tension tests. (a) A dog-bone specimen with airbrush speckle. (b) A dog-bone specimen clamped on the uTS microscopic testing system.

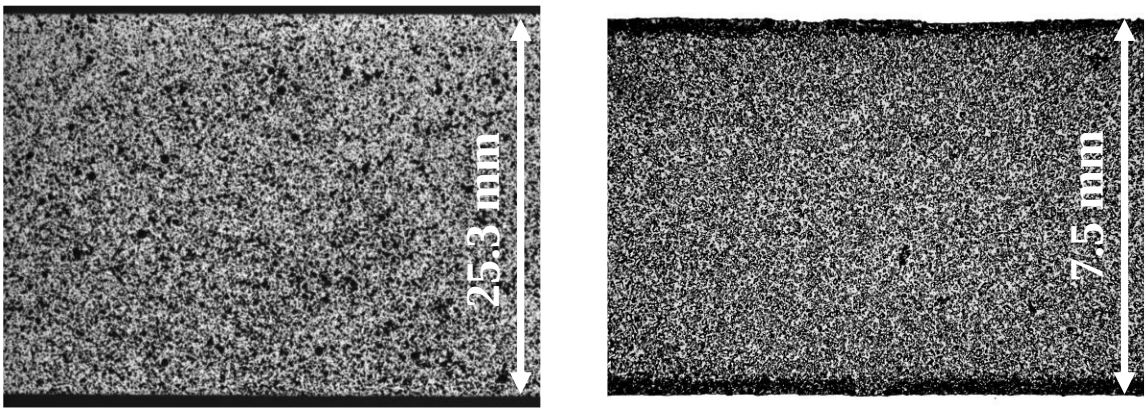

(a) (b)

Figure 4. Different scales of speckles for DIC measurement on the specimens. (a) A macroscopic specimen. (b) A microscopic specimen.

4.0 Experimental Results

The following sections of this report describe the methodology and results from each of the performed tests. All test sets targeted a nominal test duration of 600 seconds or 10 minutes. Capturing DIC images at a rate of 1 Hz provided ample time to ensure that the stress-strain development was captured with minimized discontinuous behavior. For test sets conducted using the macroscopic testing methodology, load data synchronized to the DIC imaging was captured at a rate of 20 Hz. A redundant set of load-displacement data was captured through the load cell of the Shimadzu AGX-V2 at a rate of 100 Hz. This redundant data set was synchronized with the load data captured at 20 Hz during post-processing analysis. For tests conducted with the microscopic and hybrid methodologies (implementing the macroscopic camera lens with the Psylotech µTS test frame), DIC imaging was again captured at 1 Hz, with synchronized load-displacement data being captured from the load-cell system at a rate of 20 Hz. The microscopic method was successfully applied to 90° tension tests. This methodology was applied to all of the other tests as well, but it was not as effective for the 90° tests due to limitations with available fixtures and the testing system's 10 kN load capacity, which prevented meaningful microscopic data from being gathered from the other tests. Also, for the V-notch shear tests, the field of view was not large enough to capture both sides of the specimen. For this reason, the hybrid methodology was developed. As only one set of load-displacement data was captured, no post-processing synchronization was required. As previously mentioned, the goal of this experimental work is to acquire the full field stress-strain curves which are not provided in the NCAMP test report (Ref. 13). The pointwise property data obtained from these tests, however, is compared to the pointwise, scalar material properties of T700GC/LMPAEK reported in the NCAMP test report as a check for the results presented in this report.

4.1 Longitudinal Tension (T1)

Tension tests were performed in the 0° direction utilizing the macroscopic testing framework. Coupons were created using the nominal ASTM-recommended dimensions for 0° unidirectional composite tests, as found in D3039/D3039M-17. Table 2 shows the nominal dimensions used during each of these tests. Additionally, due to the texture of the Shimadzu wedge grips, the supporting tab material was epoxied to the coupons. The principal axes are shown above in Table 1, along with these specimens' loading and fiber directions. Figure 5 depicts the stress-strain response of each specimen. In Table 3, the mechanical properties of each longitudinal tension test can be seen along with the failure mode. The failure modes are

taken from the ASTM standard D3039/D3039M-17 and represent how each specimen failed. For the 0° tensile tests, the failure modes are included here: XGV (eXplosive Gauge Various), M(LS)AB (Multi-mode (Lateral longitudinal Splitting) At grip/tab Bottom), SGM (longitudinal Splitting Gauge), SGL (longitudinal Splitting Gauge Left), and SGR (longitudinal Splitting Gauge Right). Due to the fiber direction in these tests, longitudinal splitting is an acceptable failure mode from the ASTM standard. Each failure mode is typical for these tests; no unexpected failures were observed. The list of material properties obtained includes the elastic modulus and strength. The elastic modulus was captured by measuring the slope of the elastic region of the stress-strain curves from each test. The strength was determined by taking the maximum stress value during each test. The stress-strain curves are primarily linear elastic until failure, which means that a plastic Poisson ratio cannot be calculated from these tests, as they stay in the elastic region.

Table 2. Nominal dimensions for 0° unidirectional composite tensile testing

Fiber Orientation	Width, mm [in.]	Overall Length, mm [in.]	Thickness, mm [in.]	Tab Length, mm [in.]	Tab Thickness, mm [in.]	Tab Bevel Angle, °
0° unidirectional	15 [0.5]	250 [10.0]	1.0 [0.40]	56 [2.25]	3 [0.118]	7

Overall, the modulus data showed reasonable consistency among the tests for longitudinal tension. These tests showed approximately a 10% difference in average modulus from the data published by NCAMP. Interestingly, Specimen 3 exhibited early softening, which can be seen in Figure 5, noting some nonlinearity at the end of the curve. This result could be due to early fiber splitting, as longitudinal splitting was seen from this test. However, Specimen 3 showed a similar strength value to the other tests. Additionally, Specimen 4 had a much higher strength than was observed in both the other tests and in the given NCAMP value. This discrepancy could be attributed to potential out-of-plane deformation bias in the 2D DIC system. Although such deformations are likely limited, they could still contribute to the observed variation among the stress-strain curves of individual coupons. However, the other specimens showed a good correlation in strength and had a slightly larger average than the data provided by NCAMP. These tests showed a slightly larger average strength than the NCAMP values, with approximately an 8% difference.

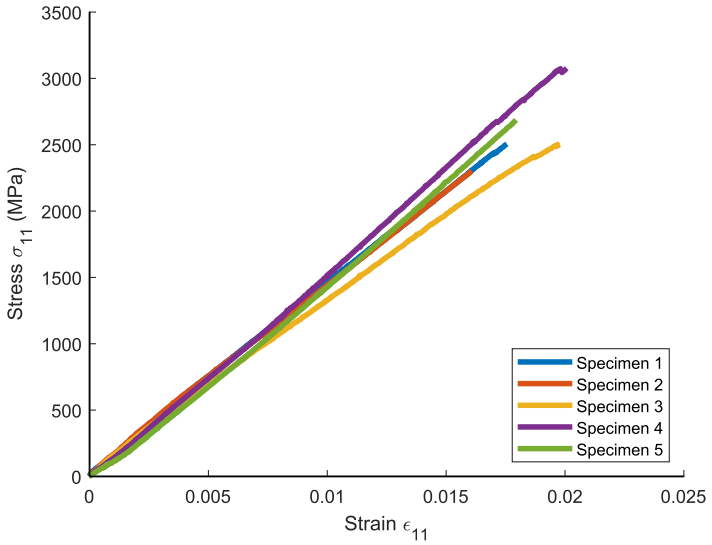

Figure 5. 0° unidirectional composite tensile testing results shown in plots representing the axial stress-axial strain curve

Table 3. Summary for 0° unidirectional composite tensile testing

Specimen	Modulus (GPa)			Strength (MPa)			Failure Mode
	Test	NCAMP	% Difference	Test	NCAMP	% Difference	
Specimen 1	143.5	130.5	9.96%	2506	2422.1	3.46%	XGV
Specimen 2	140.7	130.5	7.82%	2303.4	2422.1	-4.90%	M(LS)AB
Specimen 3	127.6	130.5	-2.22%	2501.9	2422.1	3.29%	SGM
Specimen 4	157.3	130.5	20.54%	3076.8	2422.1	27.03%	SGL
Specimen 5	152	130.5	16.48%	2687	2422.1	10.94%	SGR
Average	144.2	130.5	10.51%	2615	2422.1	7.96%	-

4.2 Transverse Tension (T2)

Tension tests were performed in the 90° direction utilizing the macroscopic and microscopic testing frameworks. The microscopic testing utilized the combined capabilities of the Psylotech µTS test frame and the Olympus microscope to provide very high-definition stress-strain data. This test set used the "dog-bone" style coupons described above in section 3.2 of this report. The principal axes are shown in Table 1, along with the loading and fiber directions of these tests. Tables 4 and 5a show the nominal dimensions used during each of these tests. Figure 6 depicts the stress-strain response of each specimen. In the stress-strain curves for these transverse tension tests, nonlinearity is demonstrated. This result is a representation of the plasticity perpendicular to the loading direction of the material. This will be important for calculating the plastic Poisson ratios seen later in this report. In Table 6, the mechanical properties of each transverse tension test can be seen along with the failure mode. The modulus values from this round of testing showed good correlation between each test; however, there is some variation in the strengths. This result could be due to the matrix material having a much more brittle fracture at a much lower load than the fiber failure.

Table 4. Nominal dimensions for 90° unidirectional fiber macroscopic tensile testing

Fiber Orientation	Width, mm [in.]	Overall Length, mm [in.]	Thickness, mm [in.]	Tab Length, mm [in.]	Tab Thickness, mm [in.]	Tab Bevel Angle, °
90° unidirectional	25 [1.0]	175 [7.0]	2.3 [0.09]	35 [1.0]	0.8 [0.031]	90

Table 5. Nominal dimensions for 90° unidirectional fiber microscopic tensile testing

Fiber Orientation	Width, mm [in.]	Gauge Length, mm [in.]	Thickness, mm [in.]	Tab Length, mm [in.]	Tab Thickness, mm [in.]	Tab Bevel Angle, °
90° unidirectional	7.5 [0.295]	25 [0.98]	2 [0.079]	-	-	-

Table 6. Summary for 90° unidirectional fiber tensile testing

Specimen	Modulus (GPa)			Strength (MPa)			Failure Mode
	Test	NCAMP	% Difference	Test	NCAMP	% Difference	
Micro 1	8.85	9.09	-2.64%	83.61	94.3	-11.34%	LGT
Micro 2	8.39	9.09	-7.70%	86.5	94.3	-8.27%	LGT
Micro 3	8.77	9.09	-3.52%	85.92	94.3	-8.89%	LGT
Micro 4	8.54	9.09	-6.05%	92.15	94.3	-2.28%	LGT
Micro 5	8.33	9.09	-8.36%	80.03	94.3	-15.13%	LGT
Macro 1	8.37	9.09	-7.92%	96.55	94.3	2.39%	LAT
Macro 2	9.61	9.09	5.72%	74.35	94.3	-21.16%	LGM
Macro 3	9.26	9.09	1.87%	72.83	94.3	-22.77%	LGT
Macro 4	9.17	9.09	0.88%	78.81	94.3	-16.43%	LGT
Average	8.81	9.09	-3.08%	83.42	94.3	-11.54%	-

The failure modes are taken from the ASTM standard D3039/D3039M-17 and represent how each specimen failed. For example, a lateral gauge top failure was seen the most from this test group and was represented by LGT. More details can be found in the ASTM standard; however, for completeness, the abbreviations for failure modes are listed here: LGT (Lateral Gauge Top), LAT (Lateral At grip/tab Top), and LGM (Lateral Gauge Middle). For this test set the only failure mode that is not ideal is the LAT. Failure at the grips or tabs is generally considered a poor failure and could be due to a flaw in the tabbing procedure.

The multi-scale testing showed a close correlation between both methodologies, with the microscopic testing acquiring noticeably less background noise during testing. This methodology allowed for a much smoother data curve, which in turn sped up the post-processing analysis while simultaneously using less material per test. Linear regression analyses yielded results that proved similar to the nominal data values published for this material in the NCAMP study. Testing shows a 3% modulus difference and a 12% difference in the strength for transverse tension between these test results and the NCAMP values. The stress-strain curves gathered from the transverse tension tests show some non-linearity, which is important for the MAT 213 characterization process and calculating the plastic Poisson ratios.

The capabilities presented using the Psylotech µTS test frame in the microscopic tests proved especially useful when analyzing the lateral strains in the *y*-direction, such as those strains developed via deformations due to Poisson's ratio. This testing methodology is an integral part of the analysis process, as computing the plastic Poisson's ratio requires high-fidelity data in the plastic regime of the stress-strain curve. The high-definition capture provided noticeably less noise in data acquisition, allowing a faster post-processing analysis for properties such as the modulus of elasticity and Poisson's ratio. This effect can be

seen in Figure 7, which shows the plots of the Poisson strains gathered from the microscopic tests. There is still some noise seen, though it is expected because the strains are so small. Additionally, each data set in the microscopic regime was produced using less overall material than a comparable test with the macroscopic framework, allowing a larger number of tests to be completed. Finally, given that tests conducted with the Psylotech μTS test frame did not require epoxied grip tabs, the total time required to prepare and perform a test was lowered, providing quality data at a much faster rate than previously possible.

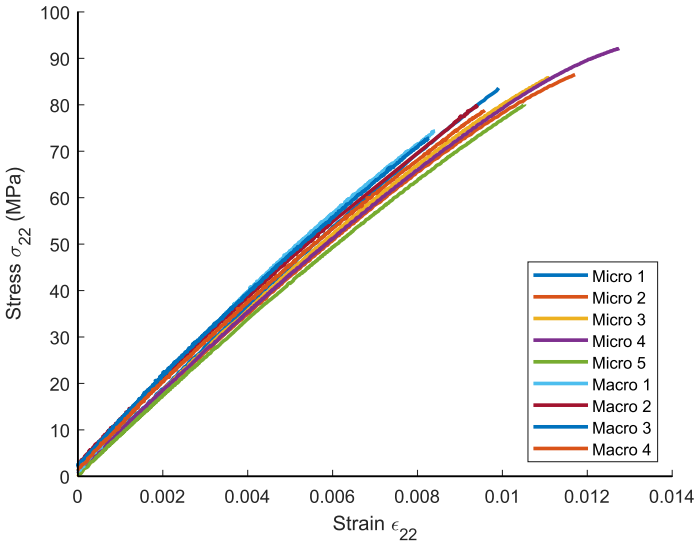

Figure 6. 90° unidirectional composite tensile testing results shown in plots representing the axial stress-axial strain curves

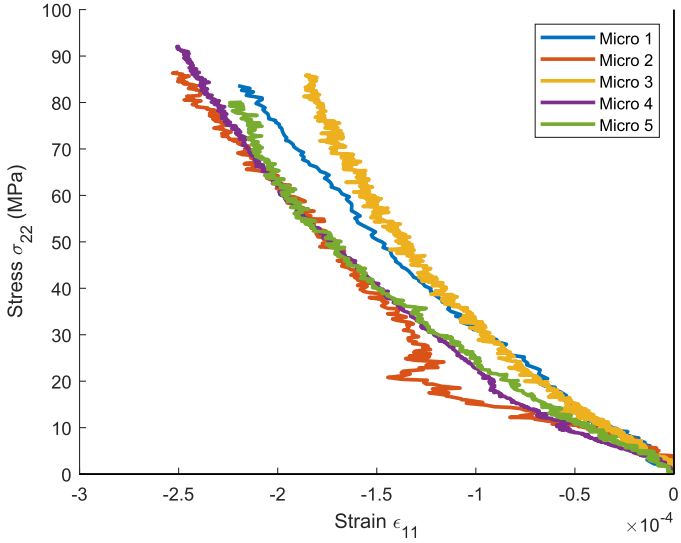

Figure 7. 90° unidirectional composite tensile testing results shown in plots representing the axial stress-Poisson strain curves for microscopic specimens

4.3 Longitudinal Compression (C1)

Compression tests were performed in the 0° direction utilizing the macroscopic testing framework. These tests used the combined loading compression (CLC) fixture from Wyoming Test Fixtures (Ref 22) oriented on the Shimadzu test frame to allow viewing of both the gauge section and the supported sections. This method was used to verify that the fracture occurred in the gauge section during testing. The gauge section dimensions were sized by referencing the nominal values for the material from the NCAMP data and ensuring a sizeable margin between the compressive fracture load and the required load for buckling. The dimensions of these specimens were changed from the ASTM standards to avoid reaching the buckling stress of the beam. Table 7 shows the nominal dimensions used during each of these tests. The principal axes are shown above in Table 1, along with the tests' loading and fiber directions. Figure 8 depicts the stress-strain response of each specimen. Table 8 contains the material properties for modulus and strength, as well as the failure modes from ASTM standard D6641/D6641M-23 for each test. The full list can be found in the ASTM manual mentioned previously. Here, the abbreviations for the 0° compression failure modes are as follows: HIM (tHrough-thickness Inside grip/tab Middle), CIB (end-Crushing Inside grip/tab Bottom), and CIT (end-Crushing Inside grip/tab Top). The strength values for four of the tests showed general agreement, with the exceptions of Specimens 3 and 4. Specimen 3 failed at a much higher strength than expected, and Specimen 4 failed at a much lower strength than expected. These results could be due to their failure modes. Specimen 3 had a unique failure mode compared to the other tests. All the specimens failed inside the grips or tabs in the tests, and some showed end crushing. These are all unacceptable failure modes specified in the ASTM manual. Given the difficulties in inducing the desired 0° compressive failure modes, NCAMP reported no compressive strength value. As such, no comparison is made for this material property in Table 8 below. However, these tests closely mirrored the 0° compressive modulus reported by NCAMP. The modulus results from these tests showed a less than 3% difference from the NCAMP data provided.

Table 7. Nominal dimensions for 0° unidirectional composite compression testing

Fiber Orientation	Width, mm [in.]	Gauge Length, mm [in.]	Thickness, mm [in.]	Tab Length, mm [in.]	Tab Thickness, mm [in.]	Tab Bevel Angle, °
0° unidirectional	9.4 [0.37]	11.4 [0.45]	4.5 [0.177]	-	-	-

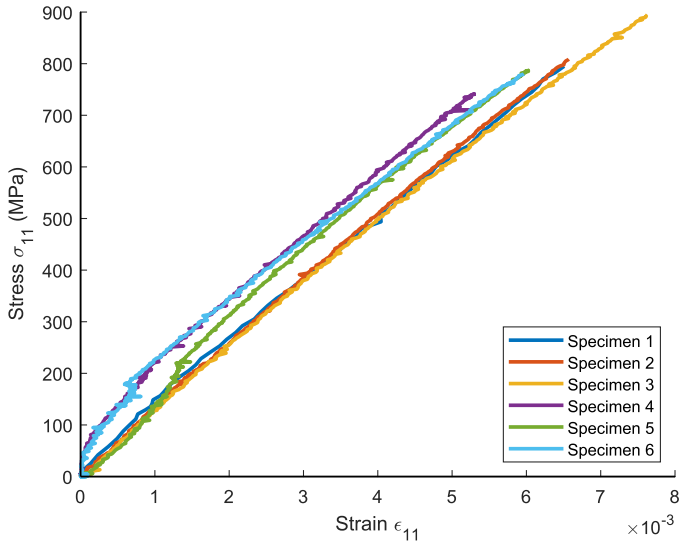

Figure 8. 0° unidirectional composite compression testing results shown in plots representing the axial stress-axial strain curves

Table 8. Summary for 0° unidirectional composite compression testing

Specimen	Modulus (GPa)			Strength (MPa)			Failure Mode
	Test	NCAMP	% Difference	Test	NCAMP	% Difference	
Specimen 1	117.5	116.8	0.60%	795.1	-	-	HIM
Specimen 2	117.5	116.8	0.60%	780.5	-	-	HIM
Specimen 3	120.7	116.8	3.34%	894.3	-	-	CIB
Specimen 4	124.6	116.8	6.68%	741.6	-	-	CIT
Specimen 5	122.1	116.8	4.54%	787.4	-	-	CIT
Specimen 6	116.4	116.8	-0.34%	780.5	-	-	HIM
Average	119.8	116.8	2.57%	796.6	-	-	-

4.4 Transverse Compression (C2)

Compression tests were performed in the 90° direction utilizing the macroscopic testing framework. Table 9 shows the nominal dimensions used during each of these tests. The principal axes are shown above in Table 1 along with these tests' loading and fiber directions. Figure 9 depicts the stress-strain curves of each specimen. Similar to the T2 stress-strain curves, these test results also show non-linearity, which is important when creating a MAT 213 material card. The elastic region for this test was defined based on the onset of failure progression rather than the conventional 0.2% offset criterion, as the stress-strain response exhibited a linear regime extending beyond 0.2% strain. The elastic region cutoff was selected at the point where the stress-strain curve began to deviate from the linear regime. This methodology was applied to other tests exhibiting nonlinear stress-strain behavior and was used in the calculation of non-associative flow-rule coefficients, which are discussed in Section 5.0. In Table 10, the mechanical properties of each transverse compression test can be seen along with the failure modes seen from this test set. The failure modes are taken from the ASTM standard D3039/D3039M-17 and are listed here: AGM

(Angled Gauge Middle) and EGM (Euler buckling Gauge Middle). These failure modes and locations are acceptable according to the ASTM manual and show that the specimens were manufactured well, and the tests were performed properly. The conducted tests showed a close correlation to all respective values published by NCAMP. To obtain the compressive modulus in this direction, the linear elastic portion of the stress-strain response curve was used for the linear regression analysis. The modulus values show good agreement within this test set, with the exception of Specimens 3 and 4, which were slightly higher than the others. When looking at the strength values, there appears to be two groups in the test set. This result is because Specimens 1 and 2 were cut from a different panel than Specimens 3 through 5, which resulted in Specimens 1 and 2 failing at a higher strength (40 MPa higher) than Specimens 3-5. Overall, the modulus values presented below show a less than 1% difference from the NCAMP values, and the strength values were a little less than 5% different from those provided by NCAMP.

Table 9. Nominal dimensions for 90° unidirectional composite compression testing

Fiber Orientation	Width, mm [in.]	Overall Length, mm [in.]	Thickness, mm [in.]	Tab Length, mm [in.]	Tab Thickness, mm [in.]	Tab Bevel Angle, °
90° unidirectional	9.4 [0.37]	12.3 [0.48]	2.2 [0.087]	-	-	-

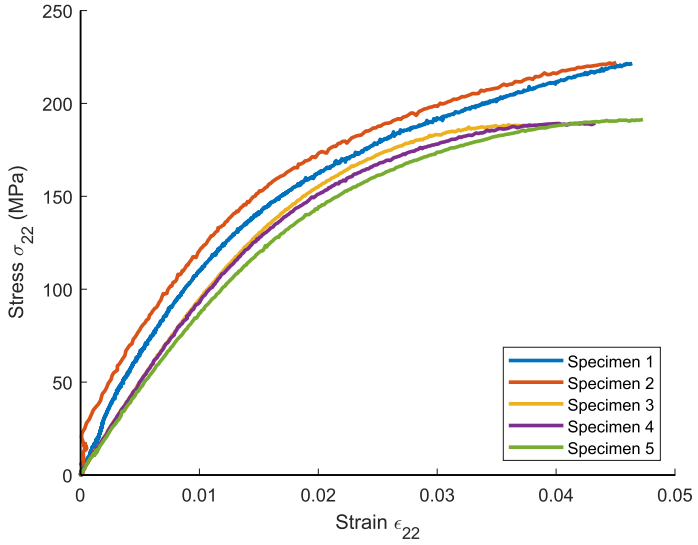

Figure 9. 90° unidirectional composite compression testing results shown in plots representing the axial stress-axial strain curves

Table 10. Summary for 90° unidirectional composite compression testing

Specimen	Modulus (GPa)			Strength (MPa)			Failure Mode
	Test	NCAMP	% Difference	Test	NCAMP	% Difference	
Specimen 1	9.12	9.24	-1.30%	221.57	212.1	4.46%	AGM
Specimen 2	8.99	9.24	-2.71%	222.14	212.1	4.73%	AGM
Specimen 3	9.74	9.24	5.41%	188.85	212.1	-10.96%	EGM
Specimen 4	9.61	9.24	4.00%	189.43	212.1	-10.69%	EGM
Specimen 5	8.92	9.24	-3.46%	191.35	212.1	-9.78%	AGM
Average	9.276	9.24	0.39%	202.66	212.1	-4.45%	-

4.5 Off-axis Tension ±45° (O12)

Tension tests were performed in the ±45° direction utilizing the macroscopic testing framework. The principal axes are shown above in Table 1 along with these tests' loading and fiber directions. These tests cannot be used directly for MAT 213 characterization; however, they are still useful for comparing test results with the NCAMP data. This test configuration is frequently used to characterize the in-plane shear response of a composite; however, the tests done for this study were not used for this purpose. This test method for in-plane shear (IPS) is outlined in the ASTM manual and is the same test performed by NCAMP. Table 11 shows the nominal dimensions used during each of these tests. Figure 10 depicts the stress-strain response of each specimen. In Table 12, the mechanical properties of each off-axis tension test can be seen along with the failure mode. The failure modes are taken from the ASTM standard D3039/D3039M-17 for tensile tests because the standard D3518/D3518M-18 used for this test set does not provide failure modes. Each of these specimens failed with MGM (Multi-mode Gauge Middle). This failure mode is acceptable per ASTM standards. The modulus and strength values showed a high level of agreement when compared to each other for these tests, as shown in Table 12 and Figure 10 below. As a result, each test nearly overlaps in the stress-strain plot. The modulus values from these tests differed by approximately 6% relative to the NCAMP data. The 0.2% and 5% offset strengths were determined in accordance with ASTM D3518/D3518M-18. The 0.2% offset stress, which refers to the stress level where the plastic strain is determined to be equal to 0.2%, is a common method to distinguish between the elastic and plastic regions. The 5% offset stress, which refers to the stress level where the plastic strain is determined to be equal to 5%, is used in the ASTM manual as the maximum shear stress. Both values exceed those reported by NCAMP, with the 0.2% offset stress averaging 16% higher and the 5% offset stress averaging 17% higher. Overall, among the test specimens, the 0.2% offset and the 5% offset stresses are relatively consistent with one another, showing only moderate variation.

Table 11. Nominal dimensions for ±45° unidirectional composite tensile testing

Fiber Orientation	Width, mm [in.]	Overall Length, mm [in.]	Thickness, mm [in.]	Tab Length, mm [in.]	Tab Thickness, mm [in.]	Tab Bevel Angle, °
90° unidirectional	22.5 [1.0]	250 [10.0]	1.25 [0.05]	35 [1.0]	3 [0.118]	7

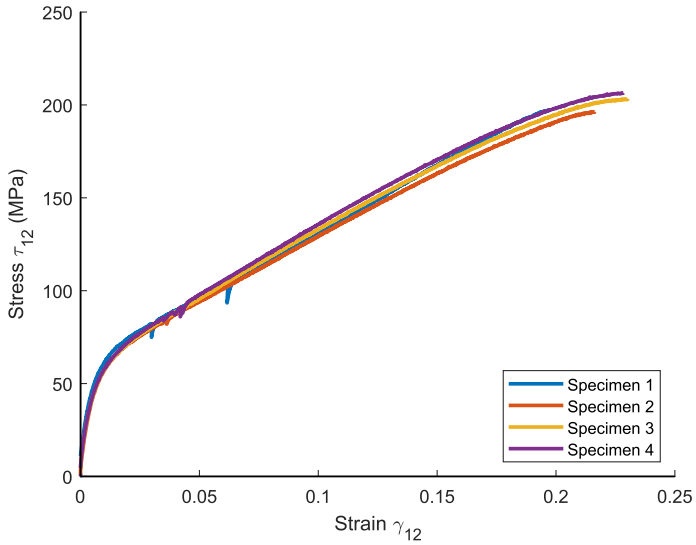

Figure 10. ±45° unidirectional composite tensile testing results shown in plots representing the shear stress-shear strain curves

Table 12. Summary for ±45° unidirectional composite tensile testing

SP*	Modulus (GPa)			0.2% Offset Strength (MPa)			5% Offset Strength (MPa)			Failure Mode
	Test	NCAMP	% Dif†	Test	NCAMP	% Dif	Test	NCAMP	% Dif	
SP 1	4.59	4.65	-1.29	45.77	37.49	22.09	78.09	65.53	19.17	MGM
SP 2	4.23	4.65	-9.03	43.71	37.49	16.59	75.40	65.53	15.06	MGM
SP 3	4.35	4.65	-6.45	42.13	37.49	12.38	76.24	65.53	16.34	MGM
SP 4	4.34	4.65	-6.67	42.85	37.49	14.30	77.13	65.53	17.70	MGM
Avg‡	4.38	4.65	-5.86	43.62	37.49	16.34	76.72	65.53	17.07	-

*SP: Specimen, †Dif: Difference, ‡Avg: Average

4.6 Longitudinal In-Plane Shear (S12)

In-plane shear tests were performed in the 0° direction utilizing the hybrid testing methodology, which utilizes the macroscopic camera lens with the Psylotech µTS test frame. This methodology allowed complete viewing of the entire speckle pattern of the coupon for the whole test duration. Table 13 shows the nominal dimensions used during each of these tests. Figure 11 depicts the shear stress-shear strain response of each specimen. In Table 14, the mechanical properties of each longitudinal in-plane shear test can be seen along with the failure mode from the ASTM standard D5379/D5379M-19e1. The shear moduli are not included for these tests because the moduli were not consistent, and the results from section 4.5 (Off-axis Tension) are consistent and closer to the data from NCAMP. These specimens failed with the mode HGN (Horizontal cracking between Notches). According to the ASTM manual, HGN is a typical acceptable failure mode. Each of these tests failed at relatively similar strengths. It is important to note that the small dips seen in the stress-strain curves could be from the small cracks that formed due to minor fiber breakage before complete failure. These tests resulted in an average strength value approximately 20% higher than those reported by NCAMP. However, it needs to be noted that NCAMP used an alternative method, specifically the ASTM D3846 In-Plane Shear-Double Notch shear test which could have led to

that underestimation. The method to determine the longitudinal in-plane shear conducted for this study is a typical shear test, but there could be some question as to whether this test results in pure shear, which is necessary for a MAT 213 input card. Instead, the S21 test was implemented for the collection of shear data.

Table 13. Nominal dimensions for 0° unidirectional composite V-notched shear beam testing

Fiber Orientation	Width, mm [in.]	Overall Length, mm [in.]	Thickness, mm [in.]	Center Width, mm [in.]	Tab Thickness, mm [in.]	Tab Bevel Angle, °
90° unidirectional	19 [0.75]	76 [3.0]	2.25 [0.088]	11.4 [0.45]	-	-

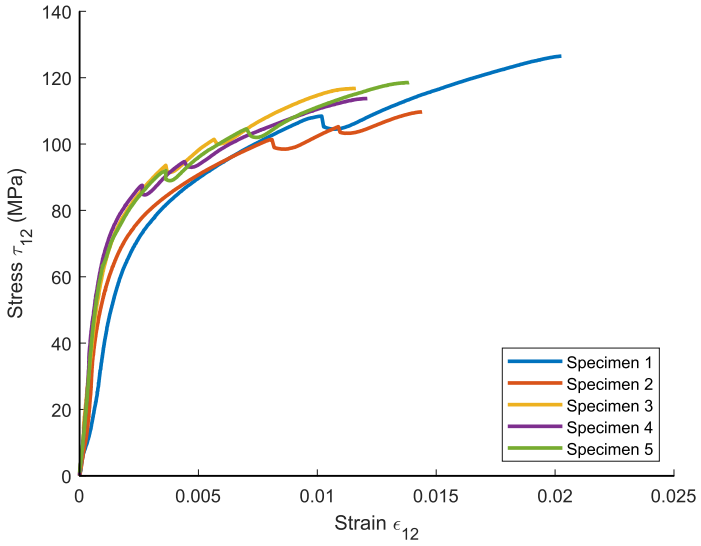

Figure 11. 0° unidirectional composite V-notched shear beam testing results shown in plots representing the shear stress-shear strain curves

Table 14. Summary for 0° unidirectional composite V-notched shear beam testing

Specimen	Strength (MPa)			Failure Mode
	Test	NCAMP	% Difference	
Specimen 1	126.5	97.2	30.14%	HGN
Specimen 2	109.7	97.2	12.86%	HGN
Specimen 3	116.8	97.2	20.16%	HGN
Specimen 4	113.7	97.2	16.98%	HGN
Specimen 5	118.6	97.2	22.02%	HGN
Average	117.06	97.2	20.43%	-

4.7 Transverse In-plane Shear (S21)

In-plane shear tests were performed in the 90° direction utilizing the hybrid testing methodology, which incorporates the macroscopic camera lens with the Psylotech µTS test frame, which allowed

complete viewing of the entire speckle pattern of the coupon for the whole test duration. The S21 tests were performed along with the S12 tests as a comparison of the strength values. Also, the S21 test could offer a better representation of pure shear than the S12 test due to the shear fracture occurring in the matrix between fibers.

Table 15 shows the nominal dimensions used during each of these tests. The test results are presented in Figure 12 in the form of the stress-strain curves. In Table 16, the mechanical properties of each longitudinal in-plane shear test are presented, along with the corresponding failure mode. As mentioned previously, the modulus values are not included for these tests, as the Off-axis Tension ±45° tests showed better results. The failure modes for these tests are taken from the ASTM standard D5379/D5379M-19e1. This test set saw only one failure mode, VGN (Vertical cracking Gauge section between Notches). This mode of failure is expected for these tests and is an acceptable failure mode per ASTM standards. Examining the results from this test, it is notable that each test failed at similar strength values, despite failure occurring at different strains. This set of stress-strain curves does not have the dips from fiber breakage (seen in the S12 tests), as the failure is a clean break in the matrix. The strength values are lower than those seen in the S12 tests, which could be due to the fibers being much harder to break than the matrix. The strength results for this test set showed a difference of approximately 5% as compared to the NCAMP data, which is much closer to the NCAMP values than the previous S12 tests.

Table 15. Nominal dimensions for 90° unidirectional composite V-notched shear beam testing

Fiber Orientation	Width, mm [in.]	Overall Length, mm [in.]	Thickness, mm [in.]	Center Width, mm [in.]	Tab Thickness, mm [in.]	Tab Bevel Angle, °
90° unidirectional	19 [0.75]	76 [3.0]	4.5 [1.77]	11.4 [0.45]	-	-

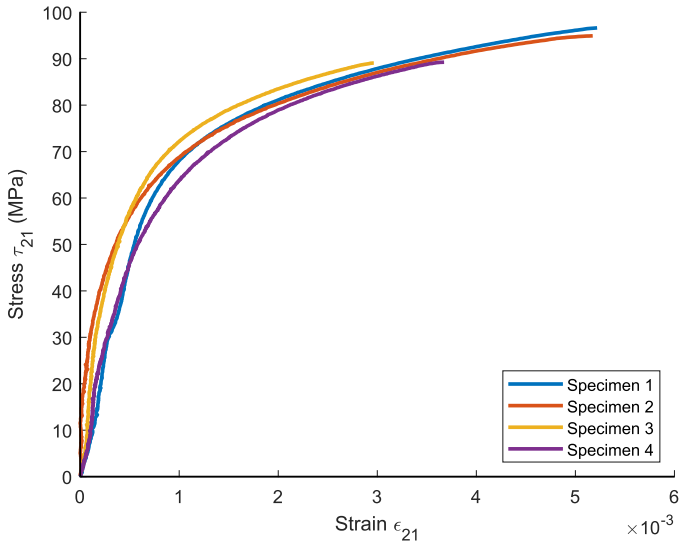

Figure 12. 90° unidirectional fiber V-notched shear beam testing results shown in plots representing the shear stress-shear strain curves

Table 16. Summary for 90° unidirectional composite V-notched shear beam testing

Specimen	Strength (MPa)			Failure Mode
	Test	NCAMP	% Difference	
Specimen 1	96.63	97.2	-0.59%	VGN
Specimen 2	94.93	97.2	-2.34%	VGN
Specimen 3	89.06	97.2	-8.37%	VGN
Specimen 4	89.24	97.2	-8.19%	VGN
Average	92.47	97.2	-4.87%	-

5.0 Characterization of Non-Associative Plasticity Flow Rule Coefficients

5.1 Theoretical Background

The MAT 213 material card requires the input of a series of non-associative plasticity flow rule coefficients, which can be determined from the plastic Poisson ratios. Details on the flow rule coefficients can be found in the MAT 213 User Guide (Ref 14). For clarity, key equations from Ref (14) are summarized below. The equation for the non-associative flow rule is expressed as follows:

$$d\varepsilon^p = d\lambda \frac{\partial h}{\partial \sigma} \tag{1}$$

where λ is the scalar plastic multiplier, σ_{ij} is true stress, ε_{ij}^p is plastic strain, and h is the plastic potential function. This potential function is expressed as follows:

$$h^2 = H_{11}\sigma_{11}^2 + H_{22}\sigma_{22}^2 + H_{33}\sigma_{33}^2 + 2H_{12}\sigma_{11}\sigma_{22} + 2H_{23}\sigma_{22}\sigma_{33} + 2H_{13}\sigma_{11}\sigma_{33} + H_{44}\sigma_{12}^2 + H_{55}\sigma_{23}^2 + H_{66}\sigma_{13}^2 \tag{2}$$

where the H_{ij} terms are independent coefficients, which are assumed to remain constant. Equations (3) through (8) show the nominal relations between the flow rule coefficients and the plastic Poisson ratios, where the $d\varepsilon_{ij}^p$ terms are the components of the increments in plastic strain.

$$\nu_{xy}^p|_{\theta=0^\circ} = \nu_{12}^p = -\frac{d\varepsilon_{22}^p}{d\varepsilon_{11}^p} = -\frac{H_{12}}{H_{11}} \tag{3}$$

$$\nu_{xy}^p|_{\theta=90^\circ} = \nu_{21}^p = -\frac{d\varepsilon_{11}^p}{d\varepsilon_{22}^p} = -\frac{H_{12}}{H_{22}} \tag{4}$$

$$\nu_{xy}^p|_{\theta=0^\circ} = \nu_{23}^p = -\frac{d\varepsilon_{33}^p}{d\varepsilon_{22}^p} = -\frac{H_{23}}{H_{22}} \tag{5}$$

$$\nu_{xy}^{p}|_{\theta=90^{\circ}} = \nu_{32}^{p} = -\frac{d\varepsilon_{22}^{p}}{d\varepsilon_{33}^{p}} = -\frac{H_{23}}{H_{33}} \tag{6}$$

$$\nu_{xy}^{p}|_{\theta=0^{\circ}} = \nu_{13}^{p} = -\frac{d\varepsilon_{33}^{p}}{d\varepsilon_{11}^{p}} = -\frac{H_{13}}{H_{11}} \tag{7}$$

$$\nu_{xy}^{p}|_{\theta=90^{\circ}} = \nu_{31}^{p} = -\frac{d\varepsilon_{11}^{p}}{d\varepsilon_{33}^{p}} = -\frac{H_{13}}{H_{33}} \tag{8}$$

This report will only focus on the H_{11}, H_{22}, H_{12}, and H_{44} coefficients, as these are the only coefficients necessary for thin shell elements. For this material, it is assumed that the 0° tension and compression tests experience almost no plasticity, which can be seen in the stress-strain curves above in Figures 5 and 8. Thus, the plastic Poisson strains are only calculated from the 90° tension and compression tests.

5.2 Experimental characterization of plastic Poisson ratios

The plastic Poisson ratio values are not used explicitly in the simulations. Instead, they are used to compute the plasticity non-associative flow rule coefficients, which are required for input into MAT 213. This requirement poses a challenge, as plastic Poisson ratios are often difficult to characterize in composite materials and may not always be available. In previous publications, Ricks et al. and Buenrostro (Refs. 20 and 21) used elastic Poisson ratios to calculate the flow rule coefficients since the data needed to calculate plastic Poisson ratios is often unavailable. This method was done assuming the elastic and plastic Poisson ratios were approximately equal. The studies referenced above demonstrated that using elastic Poisson's ratios to calculate the flow rule coefficients can be a viable alternative, accurately predicting the dynamic response of the composite materials examined and highlighting the capabilities of the MAT 213 material model. Some users (Ref. 24) determined the coefficients through an optimization process; however, the work presented here intends to use a more rigorous approach by calculating plastic Poisson ratio values based on the experimental data to improve the reliability of the simulation results.

Below, Equations (9) through (12) outline the procedure used to calculate the plastic Poisson ratios. In these equations, the total strains (ε_{ij}^{t}), elastic strains (ε_{ij}^{e}), and plastic strains (ε_{ij}^{p}) are used. Equation (10), which is derived from Equation (9), is used to calculate the Poisson plastic strains. To find the value of E_{22} (elastic modulus) needed in Equations (10) and (12), a linear regression was performed on the stress-Poisson strain data, as shown in Figures 13a and 14a. The elastic Poisson ratio is calculated using Equation (11), as seen in Figures 13b and 14b. For calculating the Poisson plastic strain, Equation (12) is used.

$$\varepsilon_{22}^{t} = \varepsilon_{22}^{e} + \varepsilon_{22}^{p} \tag{9}$$

$$\varepsilon_{22}^{p} = \varepsilon_{22}^{t} - \frac{\sigma_{22}}{E_{22}} \tag{10}$$

$$\nu_{21}^{e} = -\frac{d\varepsilon_{11}^{e}}{d\varepsilon_{22}^{e}} \tag{11}$$

$$\varepsilon_{11}^{p} = \varepsilon_{11}^{t} + v_{21}^{e}\frac{\sigma_{22}}{E_{22}} \tag{12}$$

$$v_{21}^{p} = -\frac{d\varepsilon_{11}^{p}}{d\varepsilon_{22}^{p}} \tag{13}$$

To validate the plastic strain calculations, the results were plotted alongside the total strains. This comparison is shown for the loading direction in Figures 13c and 14c, and for the direction perpendicular to the loading in Figures 13d and 14d. The goal of this comparison is to verify that the plastic strains remain negligible before yielding and increase only after the yield point. While this behavior is visible in the tension tests, the plasticity is more prominent in the compression plots, where the divergence between total and plastic strains occurs more sharply and consistently after the yield point. This data lends confidence to the accuracy of the plastic strain computations in the compression tests and will be discussed with the results from this section. Finally, the plastic Poisson ratio, v_{21}^{p}, was calculated using Equation (13), as illustrated in Figures 13e and 14e.

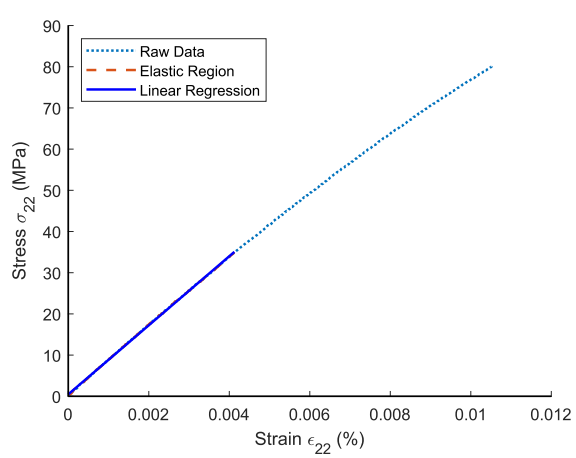

(a)

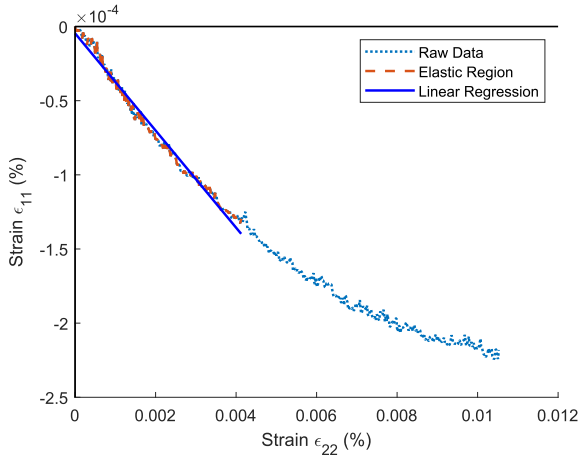

(b)

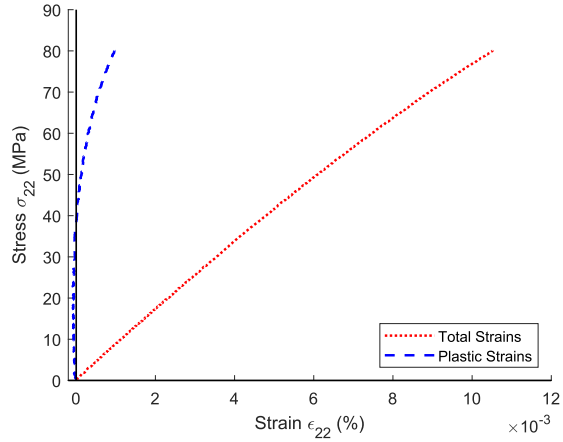

(c)

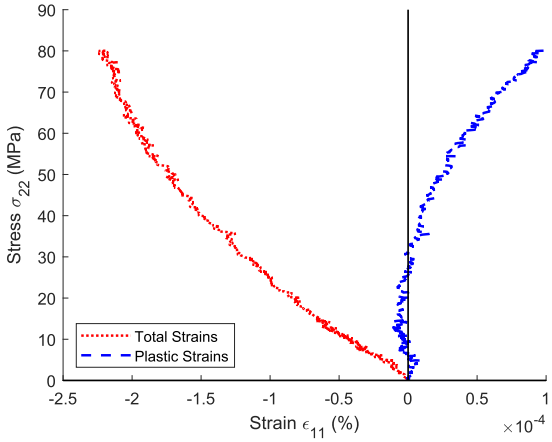

(d)

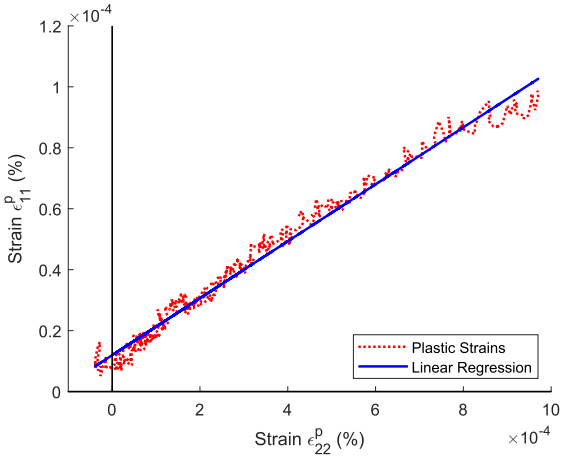

(e)

Figure 13. Steps to find elastic and plastic Poisson ratios for 90° tension. (a) Linear regression of the loading direction elastic region. (b) Linear regression to find the elastic Poisson ratio for 90° tension. (c) Elastic strains vs plastic strains in the loading direction. (d) Elastic strains vs plastic strains in the direction perpendicular to the loading. (e) Plastic strains and linear regression to calculate the plastic Poisson ratio.

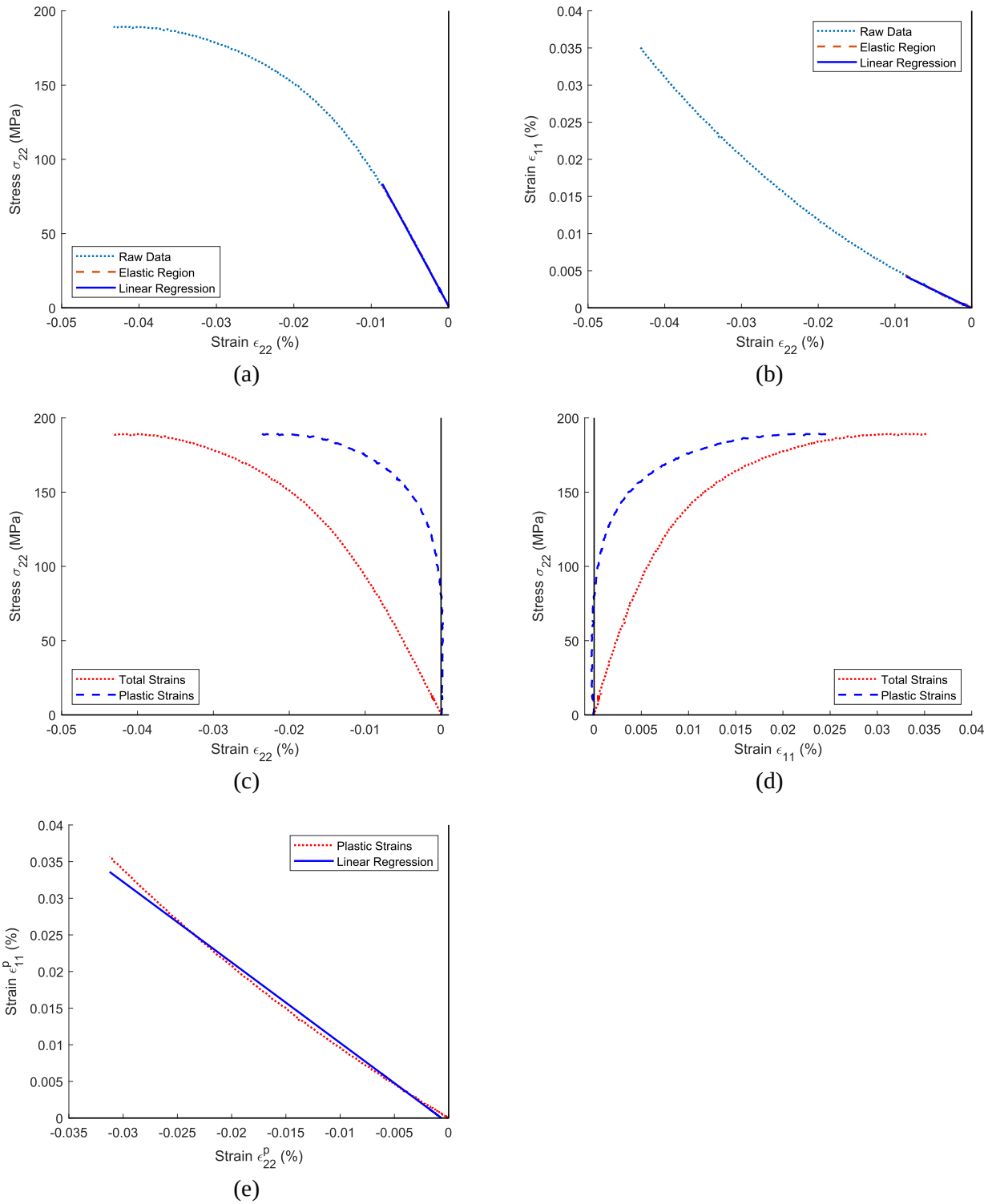

Figure 14. Steps to find elastic and plastic Poisson ratios for 90° compression. (a) Linear regression of the loading direction elastic region. (b) Linear regression to find the elastic Poisson ratio for 90° compression. (c) Elastic strains vs plastic strains in the loading direction. (d) Elastic strains vs plastic strains direction perpendicular to the loading. (e) Plastic strains and linear regression to calculate the plastic Poisson ratio.

Below in Tables 17 through 20, the elastic and plastic Poisson ratios for 0° and 90° tension and compression can be seen. As stated above, the 0° tests are assumed to have no plasticity, so the plastic Poisson ratio is not calculated. They are provided to show what values will be implemented into the material card and to compare the elastic Poisson values to those provided by NCAMP. The average for 0° tension values showed less than a 2% error for elastic Poisson ratios, and the average for 0° compression was approximately 19%. As shown in Figure 13e above, the Poisson plastic strains for 90° transverse tension tests exhibit slight hardening, which resulted in a calculated negative plastic Poisson ratio. This physically unrealistic outcome is consistently observed across all of the transverse tension tests. One possible explanation is that the small magnitude of the plastic strains caused the derived plastic Poisson ratios to appear negative when, in fact, they are negligible. Additional testing will be necessary to fully understand this behavior. These results are also a testament to how difficult it can be to experimentally determine the plastic Poisson ratios. In the meantime, the 90° compression values will be used for simulations.

Table 17. Elastic and Plastic Poisson's Ratio for 0° tensile test

Specimen	Elastic Value (ν_{12}^{e}-T)			Plastic Value (ν_{12}^{p}-T)		
	Test	NCAMP	% Difference	Test	NCAMP	% Difference
Specimen 1	0.3343	0.3371	-0.83%	-	-	-
Specimen 2	0.3228	0.3371	-4.24%	-	-	-
Specimen 3	0.3554	0.3371	5.43%	-	-	-
Specimen 4	0.3174	0.3371	-5.84%	-	-	-
Average	0.3325	0.3371	-1.37%	-	-	-

Table 18. Elastic and plastic Poisson's ratio for 0° compressive test

Specimen	Elastic Value (ν_{12}^{e}-T)			Plastic Value (ν_{12}^{p}-T)		
	Test	NCAMP	% Difference	Test	NCAMP	% Difference
Specimen 1	0.2616	0.3633	-27.99%	-	-	-
Specimen 2	0.3504	0.3633	-3.55%	-	-	-
Specimen 3	0.4075	0.3633	12.17%	-	-	-
Specimen 4	0.2665	0.3633	-26.64%	-	-	-
Specimen 5	0.238	0.3633	-34.49%	-	-	-
Specimen 6	0.2797	0.3633	-23.01%	-	-	-
Average	0.3006	0.3633	-17.25%	-	-	-

Table 19. Elastic and plastic Poisson's ratio for 90° tensile test

Specimen	Elastic Value (v_{21}^e-T)			Plastic Value (v_{21}^p-T)		
	Test	NCAMP	% Difference	Test	NCAMP	% Difference
Specimen 1	0.02784	-	-	-0.0637	-	-
Specimen 2	**0.066**	-	-	-0.2099	-	-
Specimen 3	0.02975	-	-	-0.0657	-	-
Specimen 4	0.03243	-	-	-0.0535	-	-
Specimen 5	0.03276	-	-	-0.0934	-	-
Average without outlier	0.03070	-	-	-0.0690	-	-
Average with outlier	**0.03776**	-	-	**-0.0972**	-	-

Table 20. Elastic and plastic Poisson's ratio for 90° compressive test

Specimen	Elastic Value (v_{21}^e-C)			Plastic Value (v_{21}^p-C)		
	Test	NCAMP	% Difference	Test	NCAMP	% Difference
Specimen 1	0.43627	-	-	1.1245	-	-
Specimen 2	0.61461	-	-	1.1404	-	-
Specimen 3	0.5065	-	-	1.1821	-	-
Specimen 4	0.5029	-	-	1.0986	-	-
Specimen 5	0.3965	-	-	1.0929	-	-
Average	0.491356	-	-	1.1277	-	-

5.3 Characterization of Non-Associative Plasticity Flow Rule Coefficients

To characterize the flow rule coefficients for MAT 213 input, Equations (14) and (15), taken from Ricks et al. (Ref. 20), are used to calculate the terms H_{11} and H_{12}. Consistent with the approach in Ref. 20, the 90° tension curve is treated as the master curve, and the H_{22} value is assumed to be unity, which is a common assumption also supported by the MAT 213 User Guide (Ref. 14). It is worth noting that Hoffarth (Ref. 23) and Khaled (Ref. 24) previously assumed H_{11}, H_{12}, and H_{13} to have a value of zero due to the predominantly linear elastic behavior observed in the longitudinal direction of unidirectional composites. However, the 0° compression tests presented in section 4.3 showed small nonlinearity, so the H11 and H12 values can be assumed to be nonzero. This study has made an effort to characterize these coefficients directly from test data. Specifically, the plastic Poisson ratio v_{21}^p value calculated above is used in Equation (14) to find the H_{12} value. From there, using the v_{21}^p along with v_{12}^e as a substitute for v_{12}^p in Equation (15), H_{11} is calculated. This substitution is made because plasticity is not observed in the longitudinal tests. The value for H_{44} was chosen based on guidance from Ricks et al. (Ref. 20) and previous experience with the MAT 213 material model. The calculated results are summarized in Table 21. The flow rule coefficients will be implemented into a MAT 213 model for the LMPAEK material, with simulation results compared against experimental data to evaluate the effectiveness of this approach. Ultimately, the validity of these coefficients can only be established through MAT 213 coupon test simulations, which will reveal whether the selected values yield results that are both reasonable and consistent with experimental observations.

$$H_{12} = -v_{21}^p H_{22} \tag{14}$$

$$H_{11} = \frac{v_{21}^{p}}{v_{12}^{p}} H_{22} \tag{15}$$

Table 21. Non-associative flow rule coefficients

Non-Associative Flow Rule Coefficients	Value
H_{11}	3.7882
H_{22}	1.0000
H_{12}	-1.2770
H_{44}	5.0000

6.0 Conclusion

In this study, extensive testing and analysis were carried out according to the applicable ASTM standards on the Toray Cetex® TC1225 (Ref. 10) Low-Melt PolyArylEtherKetone (LMPAEK) reinforced by T700GC-12K unidirectional carbon-fiber. Both the macroscopic and the microscopic testing frameworks were implemented during testing to gather the data needed for an LS-DYNA MAT 213 material input. Overall, the modulus and strength data from each test group showed good agreement with the data provided by the National Center for Advanced Materials Performance (NCAMP), as well as collecting the full-scale stress-strain data requisite for use in MAT 213 simulations. The elastic and plastic Poisson ratios were calculated, which provided the means to calculate the non-associative flow rule coefficients used within the MAT 213 material card. As previously noted, some researchers determined these coefficients using optimization techniques (Ref. 24) or by relying on the elastic Poisson ratios (Ref. 20). In contrast, this work was able to experimentally characterize the plastic Poisson ratios and use those values to calculate the non-associative flow rule coefficients. In the future, the LMPAEK MAT 213 material card will be developed with the results obtained from this study, and simulations will be performed to determine the effectiveness of the flow rule coefficients calculated in this report. This work has been focused on quasi-static tests, and future testing will examine the effects of a high-strain-rate response on the LMPAEK material. With both data sets available, a more comprehensive input card can be developed for LS-DYNA's MAT 213, enhancing the accuracy of material modeling in high-energy impact simulations for this material.

References

1. NASA. (2023, September 22). 20 years ago: Remembering Columbia and her crew. NASA. Retrieved May 6, 2025, from https://www.nasa.gov/history/20-years-ago-remembering-columbia-and-her-crew/
2. National Transportation Safety Board (NTSB), Aircraft Accident Report: Left Engine Failure and Subsequent Depressurization, Southwest Airlines Flight 1380, Boeing 737-7H4, N772SW, NTSB/AAR-19/03. PB2019-101439, Philadelphia, PA, 2018.
3. LS-Dyna | Livermore Software Technology Corp.. (n.d.). Retrieved May 6, 2025, from http://www.lstc.com/products/ls-dyna
4. C. Hoffarth, B. Khaled, L. Shyamsunder, S. Rajan, R. Goldberg, K. S. Carney, P. DuBois, and G. Blankenhorn. Verification and validation of a three-dimensional orthotropic plasticity constitutive model using a unidirectional composite. Fibers, 5(1), 12, 2017.
5. Goldberg, R. K., Carney, K. S., DuBois, P., Hoffarth, C., Harrington, J., Rajan, S., & Blankenhorn, G. (2016). Development of an orthotropic elasto-plastic generalized composite material model suitable for impact problems. Journal of Aerospace Engineering, 29(4), 04015083.
6. Goldberg, R. K., Carney, K. S., DuBois, P., Hoffarth, C., Khaled, B., Rajan, S., & Blankenhorn, G. (2018). Analysis and characterization of damage using a generalized composite material model suitable for impact problems. Journal of Aerospace Engineering, 31(4), 04018025.
7. HexPly® 8552. (n.d.-a). Retrieved May 6, 2025, from https://www.hexcel.com/user_area/content_media/raw/HexPly_8552_us_DataSheet.pdf
8. Justusson, B. P., Molitor, M. T., Iqbal, J. S., Rassaian, M., Ricks, T. M., & Goldberg, R. K. (2020). Overview of coupon testing of an IM7/8552 composite required to characterize high-energy impact dynamic material models. NASA Technical Memorandum, NASA/TM-2020-220498.
9. Haluza, R. T., Goldberg, R. K., Ricks, T. M., Pereira, J. M., Koudela, K. L., & Bakis, C. E. (2024). Modeling dynamic crush behavior of carbon fiber reinforced polymer composite structures using MAT 213. Composite Structures, 338, 118063.
10. Toray Cetex® TC1225. (n.d.-c). Retrieved May 6, 2025, from https://www.toraytac.com/media/3bd72fac-0406-48e4-bfc4-2ffd2398ac0c/fxj5OQ/TAC/Documents/Data_sheets/Thermoplastic/UD%20tapes,%20prepregs%20and%20laminates/Toray-Cetex-TC1225_PAEK_PDS.pdf
11. Berretta, S., Chaplin, A., Anderson, A., & McKay, R. (2022). A Technical Review of New Polyaryletherketones (PAEK) Alternatives to PEEK for Additive Manufacturing and Additive Manufacturing Composites. SAMPE Journal, January/February 2022, 32-41.
12. Raps, L., Chadwick, A. R., Schiel, I., & Schmidt, I. (2022). CF/LM-PAEK: Characterisation and sensitivity to critical process parameters for automated fibre placement. Composite Structures, 284, 115087.
13. Lian, E. (2021) Medium Toughness PAEK Thermoplastics Toray (Formerly TenCate) Cetex® TC1225 (LM PAEK) T700GC 12K T1E Unidirectional Tape 145 gsm 34% RC Qualification Material Property Data Report. NCAMP Project NPN 061701, NCAMP Test Report CAM–RP–2019–036 Rev A.
14. Rajan, S. D., Hoffarth, C., Khaled, B. & Shyamsunder, L. (2023). MAT_213 User Guide (Version 1.3.6): A User Guide for *MAT_COMPOSITE_TABULATED_PLASTICITY_DAMAGE in LS-DYNA®, [Online]. Retrieved May 6, 2025, from https://awg.ansys.com/tiki-download_file.php?fileId=2504
15. ASTM International. (2017). Standard test method for tensile properties of polymer matrix composite materials. D3039/D3039M-17 Edition. ASTM international, West Conshohocken, PA.
16. ASTM International. (2021). Standard Test Method for Compressive Properties of Polymer Matrix Composite Materials Using a Combined Loading Compression (CLC) Test Fixture. D6641/D6641M-

16e2 Edition, West Conshohocken, PA.
17. ASTM International. (2021). Standard test method for shear properties of composite materials by the V-notched beam method. D5379/D5379M-19e1 Edition. ASTM international, West Conshohocken, PA.
18. ASTM International. (2018). Standard test method for in-plane shear response of polymer matrix composite materials by tensile test of a ±45° laminate. D3518/D3518M-18 Edition. ASTM international, West Conshohocken, PA.
19. Miller, S. G., Heimann, P. J., Miller, A. J., Scheiman, D. A., & McCorkle, L. S. (2023). Manufacturing and Mechanical Testing of TC1225/LM-PAEK and TC1200/PEEK Thermoplastic Composite Panels. NASA Technical Memorandum, NASA/TM-20220015690.
20. RICKS, T. M., GOLDBERG, R. K., & PEREIRA, J. M. (2023). High-Energy Dynamic Impact Modeling of an AS4D/PEKK-FC Composite Using LS-DYNA MAT213. In Proceedings of the American Society for Composites-Thirty-Eighth Technical Conference on September 17-20, 2023, in Greater Boston, MA.
21. Buenrostro, J. (2022). Characterization of the Response of Woven Composites and Additively Manufactured Metals Defects under Intermediate Loading Rates (Order No. 29397354). [Doctoral dissertation, University of California San Diego]. Available from ProQuest Dissertations & Theses Global. (2774158522).
22. Wyoming combined loading compression test fixture (ASTM D6641). Wyoming Test Fixtures. (n.d.). Retrieved May 6, 2025, from https://wyomingtestfixtures.com/products/compression/wyoming-combined-loading-compression-test-fixture-astm-d-6641/
23. Hoffarth, C. (2016). A Generalized Orthotropic Elasto-Plastic Material Model for Impact Analysis (Order No. 10194635). [Doctoral dissertation, Arizona State University]. Available from ProQuest Dissertations & Theses Global. (1841248778).
24. Khaled, B. (2019). Experimental Characterization and Finite Element Modeling of Composites to Support a Generalized Orthotropic Elasto-plastic Damage Material Model for Impact Analysis (Order No. 13895147). Available from ProQuest Dissertations & Theses Global. (2273835258). [Doctoral dissertation, Arizona State University]. Retrieved

Appendix

The C-scan images of the T700GC/LMPAEK panels are presented in this appendix section. The images were taken immediately after the manufacturing process for quality control. Note the areas at the bottom of the $[0]_{32}$ laminate (depicted as solid white, see Figure A1a) was intended for debonding in the mid-layer for mode-II interlaminar fracture testing. The debonded part was not used in this work. The solid red color of the other laminates indicates strong adhesion between layers.

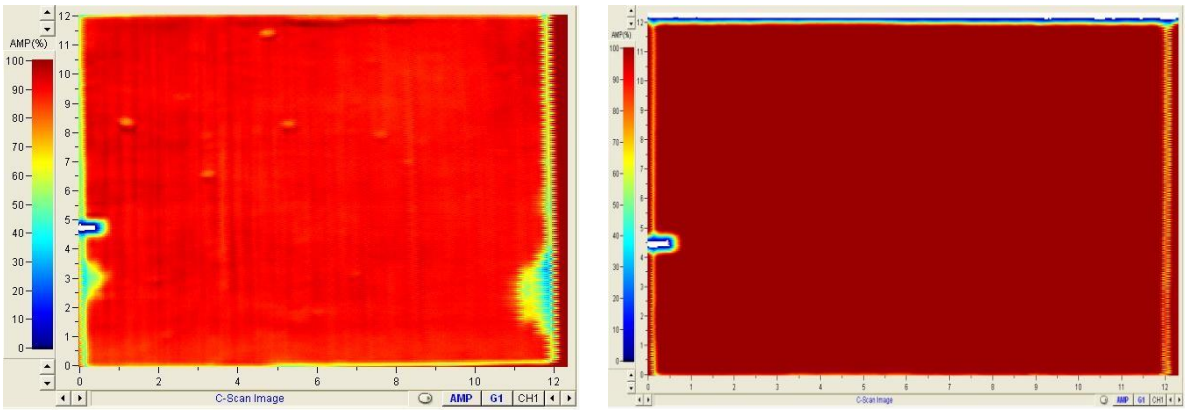

(a) (b)

Figure A2. C-scan images of two $[0]_8$ panels for the T1 tests. (a) $[0]_8$-1 panel. (b) $[0]_8$-2 panel.

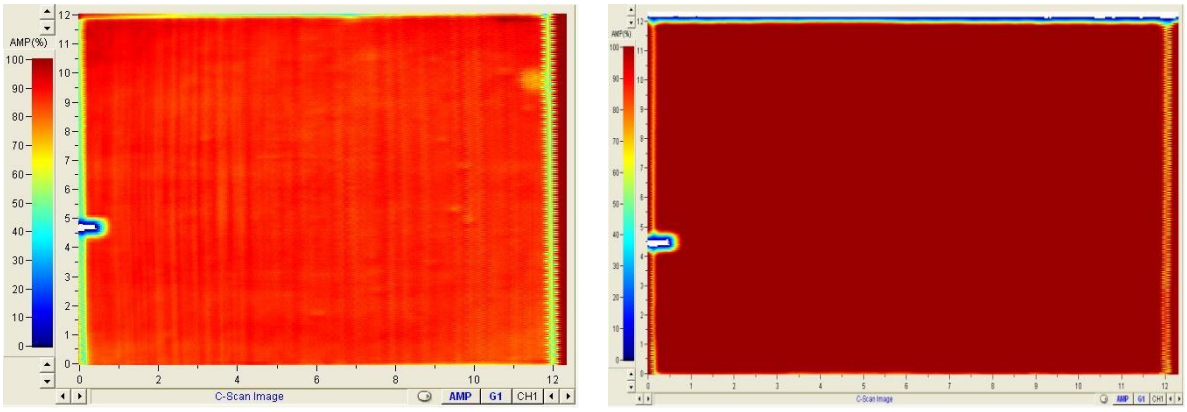

(a) (b)

Figure A3. C-scan images of two $[0]_{16}$ panels for the T2, S12, and S21 tests. (a) $[0]_{16}$-1 panel. (b) $[0]_{16}$-2 panel.

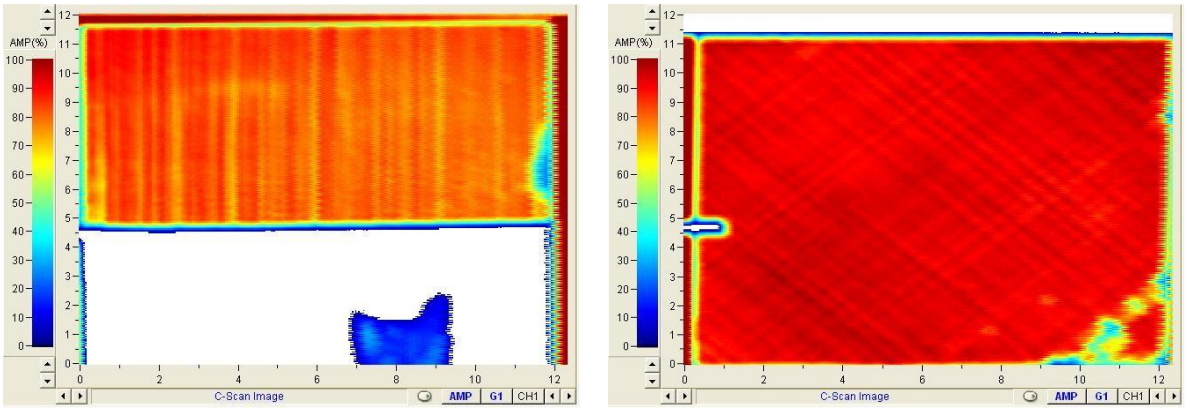

(a) (b)

Figure A4. C-scan images of the $[0]_{32}$ and $[\pm 45]_{2s}$ panels for the C1, C2, and O12 tests. (a) $[0]_{32}$ panel. (b) $[\pm 45]_{2s}$ panel.